New RAMS cloud microphysics parameterization. Part II: The two-moment scheme

Michael P. Meyers [a,*], Robert L. Walko [b], Jerry Y. Harrington [b], William R. Cotton [b]

[a] *National Weather Service, 792 Eagle Drive, Grand Junction, CO 81506, USA*
[b] *Colorado State University, Department of Atmospheric Science, Fort Collins, CO 80523, USA*

Abstract

This paper is the second in a series of articles describing the new microphysics scheme in the Regional Atmospheric Modeling System (RAMS). In this part, a new two-moment microphysical parameterization is described. The proposed scheme predicts the mixing ratio and number concentration of rain, pristine ice crystals, snow, aggregates, graupel and hail. The general gamma distribution is the basis function used for hydrometeor size in each category. Additional features include: use of stochastic collection for number concentration tendency; breakup of rain droplets formulated into the collection efficiency; diagnosis of ice crystal habit dependent on temperature and saturation; evaporation and melting of each species assuming that the smallest particles completely disappear first; and more complex shedding formulations which take into account the amount of water mass on the coalesced hydrometeor. Preliminary sensitivity testing of the new microphysical scheme in an idealized convective simulation shows that the two-moment prediction scheme allows more flexibility of the size distribution enabling the mean diameter to evolve in contrast to the one-moment scheme. Sensitivity to the prescribed input parameters such as cloud droplet concentrations and the shape parameter ν is demonstrated in the model results. © 1997 Elsevier Science B.V.

1. Introduction

With the advancing state of computer technology, atmospheric modelers are now able to incorporate more sophisticated physics into their models in the hope of gaining a better understanding of the physical controls on atmospheric processes. Cloud models

* Corresponding author. Tel.: +1 970 2437007; fax: +1 970 2570452; e-mail: mmeyers@sac.gjtnwscr.noaa.gov

specifically need to adequately represent the hydrometeor evolution over a wide variety of conditions to accurately predict the microstructure of cloud systems. Cloud modelers have two options to represent the hydrometeor spectra, explicit bin-resolving (Young, 1974; Hall, 1980; Kogan, 1991; Feingold et al., 1988, 1994) or bulk microphysical models (Lin et al., 1983; Rutledge and Hobbs, 1983, 1984; Cotton et al., 1986). Bin models divide each hydrometeor category (e.g. cloud droplets, rain, ice crystals, hail) into several bins each representing a part of the full spectrum of hydrometeor diameters and/or mass. One or more parameters for each bin are prognosed, making this approach expensive in computer time and memory. Bulk microphysical schemes represent hydrometeor size for each class with a distribution function, such as a exponential function (Kessler, 1969) or a gamma type (Walko et al., 1995; hereafter referred to as Part I) resulting in much fewer prognostic variables. Simplified formulas represent all interactions between each of the hydrometeor classes which result from the integration of the hydrometeor spectra.

Another capability of bulk microphysical schemes is the degree of sophistication used in representing the hydrometeor size spectra. In the previously mentioned bulk microphysical models, only one moment of the distribution is predicted (usually mixing ratio) while the other moments are diagnosed or prescribed. An improvement in the representation of the hydrometeor spectra has been to predict two moments of the hydrometeor distribution, namely, the mixing ratio and the number concentration, and to diagnose the mean diameter (Ziegler, 1985; Nickerson et al., 1986; Murakami, 1990; Wang and Chang, 1993; Ferrier, 1994). Srivastava (1978) noted the advantages of predicting two parameters of the hydrometeor size spectra especially in precipitation processes. Prediction of two moments of the distribution allows more degrees of freedom of the hydrometeor spectra for each category, improving prediction of complex microphysical processes. Improvements should also be expected in radar reflectivity and radiative transfer calculations, which are both dependent on the size and the number concentration of the hydrometeors, and in buoyancy-driven dynamics.

In this paper we describe the two-moment prediction scheme used in the Regional Atmospheric Modeling System (RAMS) developed at Colorado State University. This work is an extension of single-moment scheme summarized in Part I. Sensitivity tests of this new scheme in an idealized convective environment are also presented to show the versatility and capabilities of the new scheme and also to make direct comparisons to the single-moment prediction scheme results from Part I.

2. Model formulations

The reader is referred to Part I for a description of the RAMS microphysical model and model formulations of the mass tendency equations. The number concentration of each hydrometeor category is governed by the continuity equations of the form

$$\frac{\partial}{\partial t}(n) = \text{ADV}(n) + \text{TURB}(n) + \text{SEDIM}(n) + \text{SOURCE}(n) \tag{2.1}$$

where $n = [n_r, n_p, n_s, n_a, n_g, n_h]$ represents the concentration of rain, pristine ice crystals, snow, aggregates, graupel, and hail. Note that the concentration of cloud

droplets (n_c) is not predicted at this time; although tendency equations for cloud droplet concentration are being developed for use in RAMS. ADV(n) and TURB(n) represent the advective and turbulent transport of number concentration by resolved and sub-grid scale velocities in the model. SOURCE(n) represents the microphysical sources and sinks of n, and SEDIM(n) represents the local losses and gains of number concentration due to gravitational sedimentation; these are described in the following sections.

2.1. Model physics

This next section describes the SOURCE and SEDIM terms in Eq. (2.1) as applied to all prognostic mixing ratios and number concentrations for each categories.

2.1.1. Autoconversion

Auto conversion refers to the transition from cloud droplets to rain drops due to collision and coalescence of cloud droplets. Berry and Reinhardt (1974a,b) discretized the droplet distribution into precipitating and non-precipitating size categories (a radius $r = 41$ μm cutoff). They then evaluated the stochastic coalescence equation (SCE) analytically to obtain tendency equations for concentration and mixing ratio.

In RAMS the cloud droplets are distributed according to the gamma distribution and based on the diagnosed liquid water content and prescribed number concentration, a mean diameter is diagnosed. From Berry and Reinhardt (1974b) a characteristic water content L and time scale τ is defined for the auto conversion process where L/τ represents an average autoconversion rate,

$$L = 2.7 \times 10^{-2} r_c \left(\tfrac{1}{16} \times 10^{20} D_m^4 (1 + \nu)^{-0.5} - 0.4 \right) \tag{2.2}$$

and

$$\tau = \frac{3.7}{\rho r_c} \left(0.5 \times 10^6 D_m (1 + \nu)^{-0.5} - 0.75 \right)^{-1}. \tag{2.3}$$

The cloud water mixing ratio is defined as r_c, D_m is the mean diameter, and ν is the shape parameter of the size distribution. The mixing ratio tendency (mks units) can then be calculated

$$\frac{dr_r}{dt} = \frac{\rho_w}{\rho} \frac{L}{\tau} \tag{2.4}$$

where ρ_w is the density of water, ρ is the density of air. The concentration tendency can be calculated as

$$\frac{dn_r}{dt} = 3.5 \times 10^6 \frac{L}{\tau}. \tag{2.5}$$

2.1.2. Ice nuclei and crystal habit

Nucleation of pristine ice crystals may be divided into two general categories: heterogeneous nucleation, in which an ice nucleus (IN) is responsible for initializing an

ice crystal structure from vapor or liquid, and homogeneous nucleation where an IN is not involved. Parameterizations representing both heterogeneous (Meyers et al., 1992) and homogeneous nucleation (DeMott et al., 1994) are described in Part I.

To account for the variability of crystal type in different environmental conditions, the capacitance and mass-dimensional relations of pristine ice crystals and snow are allowed to vary. Since the model does not keep track of the history of all crystals, a simple diagnostic check of the ambient temperature and saturation conditions at each grid location is performed during each time-step to determine the crystal habit. Two different options in the diagnosis of pristine ice and snow crystal habit are used. The first scheme, which is intended for orographic and shallow layer clouds, assumes that the cloud top conditions dictate the crystal type throughout the layer of the cloud. A crystal habit is diagnosed at the top of each cloud layer dependent on temperature and saturation and is assumed for the cloud layer down to the bottom of the cloud. If another cloud layer is encountered below the upper cloud, a crystal type for the cloud top conditions of that particular cloud layer is diagnosed independently of the upper cloud. A more simplistic scheme is also formulated in RAMS where the crystal type is diagnosed at each grid location based on the local temperature and saturation conditions. This scheme allows variability of the crystal type in the cloud layer unlike the first scheme. All of these schemes follow a simple table lookup format based on temperature and ice supersaturation. The table formulation is based on the vapor excess and temperature dependent diagram of Fletcher (1962); these habits are given in Table 1. These schemes are compared in Section 3.2.

The habit diagnosis impacts the model in several ways. The capacitance is dependent on crystal type (Harrington et al., 1995) and may change the growth characteristics of the crystals. For instance, needles tend to grow more quickly than plates for the same environmental conditions. Different types of crystals fall at different speeds which is determined by the power law relation

$$v_t = \alpha_{vt} D^{\beta_{vt}}. \tag{2.6}$$

where D is the hydrometeor diameter and α_{vt} and β_{vt} are constants for a given crystal habit. The crystal-dependent terminal velocities impact the sedimentation of the hydrometeors. The crystal type information is also used to determine the amount of conversion to graupel due to hydrometeor collection of cloud water by pristine ice crystals and snow. The deposition scheme may be simplified for convective type clouds to assume a specific crystal type, since collection processes are dominant over depositional growth.

2.1.3. Secondary production of ice crystals

Cotton et al. (1986) discussed secondary ice production due to riming following the work of Gordon and Marwitz (1981), who developed a parameterization for the Hallet-Mossop ice multiplication theory (Hallet and Mossop, 1974). Two basic models were discussed in the Cotton et al. (1986) paper, in which they questioned whether both these processes are independent processes or just different steps in interpretation of the Hallet-Mossop experiments. If this is the case, then both equations would possibly lead to double counting the same process. Cotton et al. (1986) argued that in that case it

Table 1
Habit diagnosis as a function of S_i and T. Ice particle habits are Cl for columns, Ndl for needles, HPl for hexagonal plates, Den for dendrites, and Ros for rosettes.

S_i	$T = 0$ to -2 C	-3 to -4 C	-5 to -6 C	-7 to -9 C	-10 to -18 C	-19 to -30 C	≤ -31 C
0.1 to 1%	Cl	Cl	Cl	Cl	HPl	Cl	Cl
1 to 2%	Cl	Cl	Cl	Cl	HPl	Cl	Cl
2 to 3%	Cl	Cl	Cl	Cl	HPl	Cl	Cl
3 to 4%	Cl	Cl	Cl	Cl	HPl	Cl	Cl
4 to 5%	Cl	Cl	Cl	Cl	HPl	Cl	Cl
5 to 6%	Cl	Cl	Cl	Cl	HPl	Cl	Cl
6 to 7%	Cl	Cl	Cl	Cl	HPl	Cl	Cl
7 to 8%	Cl	Cl	Cl	Cl	HPl	Cl	Cl
8 to 9%	Cl	Cl	Ndl	Cl	HPl	Cl	Cl
> 9%	HPl	HPl	Ndl	Ndl	Den	Ndl	Ros

would be desirable to chose only one multiplication process. It was decided to use the following scheme from based on Mossop (1976),

$$\log_{10}(A/N_L) = (0.93 \log_{10} N_s - 6.0) f_1(T_s) \qquad (2.7)$$

where A is the production rate of ice particles and N_L and N_s are the collection rates of cloud droplets larger and smaller than 24 microns in diameter, respectively, determined from incomplete gamma functions multiplied by the total droplet collection rate. The Hallet-Mossop mechanism is thought to peak at $-5°C$, and be about zero above $-3°C$ and below $-8°C$. Linear interpolation then yields (Cotton et al., 1986):

$$f_1(T_s) = \begin{cases} 0; & T_s > 270.16 \\ [(T_s - 268.16)/2]; & 270.16 \geq T_s \geq 268.16 \\ [(T_s - 268.16)/3]; & 268.16 \geq T_s \geq 265.16 \\ 0; & 265.16 \geq T_s \end{cases} \qquad (2.8)$$

2.1.4. Collection

In Part I, the impact of collection on mixing ratio tendency was discussed based on Verlinde et al. (1990). Collection impacts number concentration in a similar manner to the mixing ratios, however, by predicting number concentration, other physical processes may be represented, such as self-collection of like-hydrometeors and raindrop breakup. The rate at which the number concentration N_{tx} of species x is collected into coalesced hydrometeors due to collisions with species y with concentration N_{ty} may be written as,

$$\frac{dN_{tx}}{dt} = -\frac{N_{tx} N_{ty} \pi F_p}{4} \int_0^\infty \int_0^\infty (D_x + D_y)^2 |V_{tx}(D_x) - V_{ty}(D_y)| f_{\text{gam } x}(D_x)$$

$$\times f_{\text{gam } y}(D_y) E(x, y) \mathrm{d}D_x \mathrm{d}D_y, \qquad (2.9)$$

where $E(x, y)$ is the collection efficiency, f_{gam} is the gamma distribution probability density function, and F_p is a density factor for hydrometeor fall velocity. A large number of the solutions to the integral are computed and tabulated in two-dimensional lookup tables similar to the technique used for mixing ratio as described in Part I.

The collecting hydrometeors are characterized by five different types of interactions depending on the specific impacts on the mixing ratios and number concentration tendencies of the hydrometeors. The first group of interactions is due to hydrometeor self-collection which only impacts the number concentration of the self-collecting hydrometeor. This type of interaction increases the mean particle size of the distribution with the exception of when breakup occurs during self-collection of rain. The second type of hydrometeor interaction treats ice collisions where pristine ice crystals and/or snow collect to form aggregates. This class of interactions results in a number concentration and mixing ratio tendency for each involved hydrometeor. A third class of ice-phase interactions occurs when the destination of collection between the collecting hydrometeor and the collected hydrometeor is the collecting hydrometeor. An example of this type of interaction is aggregate collection of snow. This class of collection results in a

Table 2
Collection weighting factors for interactions involving ice categories and cloud droplets

Collecting Hydrometeor	ζ	χ
snow (spatial)	1	0
snow (columnar)	1	1
aggregates	1	0
graupel	0.5	0
hail	0	0

number and mass tendency for the collected hydrometeor and a mass tendency for the collecting hydrometeor.

The next two types of collection involve ice-liquid interactions. In these collection processes the destination may be a third hydrometeor category, rain, graupel or hail. In interactions involving an ice category with the cloud droplet or rain categories, three factors determine the destination of the collection: the type and amount of colliding ice hydrometeor, the amount of rain or cloud mixing ratio collected, and the diagnosed liquid and ice contents of the species produced by the collection event after the constituents have reached thermal equilibrium. The amounts of mixing ratio, number concentration, and thermal energy produced by the collisions are divided between the input ice category (the ice category before the collection event) and a secondary ice category (the ice category into which the rimed ice is transferred), which is graupel when the interaction involves cloud water, and hail when the interaction involves rain. A simple diagnostic scheme was devised to determine the amount of collected mass transferred to the secondary ice category:

$$r_{\text{sec}} = \min\left(r_{\text{colt}}, \zeta r_{\text{liq}} + \chi r_{\text{coll}}\right) \tag{2.10}$$

where r_{sec} is the amount of mass being sent to the secondary ice category, r_{colt} is the amount of collected mass, r_{liq} is the mixing ratio of the liquid portion of the coalesced hydrometeor after the two contributors reach thermal equilibrium with each other, and r_{coll} is the amount of collected mass of the liquid categories. The ζ and χ values for each hydrometeor interaction are given in Tables 2 and 3, and these determine the transfer during collection of liquid based on the hydrometeors involved. The remaining content of the coalesced hydrometeor is retained in the input ice category. For example, a dendritic snowflake will continue to keep its identity after collecting cloud water in a dry-growth regime, but a columnar snowflake will more likely be converted over to graupel especially in a wet growth regime. Ice-rain interactions usually result in most of

Table 3
Collection weighting factors for interactions involving ice categories and cloud droplets

Collecting Hydrometeor	ζ	χ
pristine ice crystals	0	10
snow	0	5
aggregates	0	5
graupel	1	1
hail	0	0

the collected mass and number being converted to the hail category. A similar diagnostic calculation is done for the number concentration tendency due to collection:

$$n_{\text{conv}} = \max\left(0., (r_{\text{colt}} - r_{\text{ret}})/r_{\text{colt}}\right) \times n_{\text{colt}})$$ (2.11)

where n_{conv} is the number concentration tendency that is converted to the third hydrometeor category, and n_{colt} is the number of collected hydrometeors.

One of the major differences between the two-moment and one-moment schemes, besides the fact that number concentration tendencies due to collection are calculated, is the importance of D_n on the collection kernel. In the one-moment scheme the characteristic diameter of the distribution may be prescribed by the user so all collection processes are based on that fixed diameter. With the two-moment scheme, the characteristic diameter is diagnosed based on the mixing ratio and concentration of the distribution allowing for varying values of D_n of each species. Implicit in the diagnosis of D_n is the possibly wide variability of the collection kernels (v_t, cross-sectional area, collection efficiencies for each species). These changes should produce greater flexibility and a more realistic depiction of the collection process.

2.1.5. Collisional breakup

The collisional breakup parameterization assumes that filament breakup is the only active mode (Brazier-Smith et al., 1973; Low and List, 1982; Srivastava, 1978). Verlinde and Cotton (1993) parameterized the breakup coalescence efficiency into the self-collection equation. A similar approach is used in RAMS (Verlinde and Cotton, 1993) by modifying the collection efficiency by

$$E_c(D_m) = \begin{cases} 1 & \text{for } D_m < D_{\text{cut}} \\ 2 - \exp[A(D_m - D_{cut})] & D_m > D_{\text{cut}} \end{cases}$$ (2.12)

where $A = 2300$, D_m is the mean diameter (m) of the raindrop distribution, and $D_{\text{cut}} = 6 \times 10^{-4}$ m. This formulation allows the $E_c = 1.0$ for $D_m \leq 6 \times 10^{-4}$ m and decreases to $E_c < 0.0$ for $D_m > 9 \times 10^{-4}$ m. Raindrop breakup results in a number concentration tendency for the rain category.

2.1.6. Deposition and evaporation

Depositional growth for all hydrometeors follows from the vapor diffusion equation for a single hydrometeor (Pruppacher and Klett, 1978)

$$\frac{dm}{dt} = 4\pi D \psi f_{Re}(\rho_{va} - \rho_{vsh}).$$ (2.13)

where ψ is the vapor diffusivity. The ventilation coefficient f_{Re} is given by (Cotton et al., 1982)

$$f_{Re} = \left[1.0 + 0.229\left(\frac{v_t D}{V_k}\right)^{0.5}\right]S,$$ (2.14)

where S is the shape parameter. Multiplying by the distribution function

$$f_{\text{gam}}(D) = \frac{1}{\Gamma(\nu)} \left(\frac{D}{D_n} \right)^{\nu-1} \frac{1}{D_n} \exp\left[-\left(\frac{D}{D_n} \right) \right],$$ (2.15)

and integrating over the distribution gives the mass diffusion rate per cubic meter of atmosphere:

$$\frac{\overline{dm}}{dt} = N_t 4\pi\psi F_{Re} (\rho_{va} - \rho_{vsh}),$$ (2.16)

where

$$F_{Re} \equiv \int_0^\infty D f_{Re} f_{\text{gam}}(D) \, dD$$ (2.17)

is the integrated product of ventilation coefficient and diameter. It is assumed that ρ_{vsh} and therefore hydrometeor temperature is independent of diameter. All hydrometeors (with the exception of pristine ice crystals which may be converted to the snow category during vapor deposition) are assumed to grow by deposition and maintain their identity in a saturated environment.

The interaction between pristine ice crystals and snow is considered a special case since the main distinction between the two species is the size of the crystals. Both pristine ice and snow distributions may occur in either ice super-saturated or ice subsaturated conditions. During conditions of ice supersaturation, pristine ice number concentration and mass mixing ratio are transferred to the snow category by vapor depositional growth (Harrington et al., 1995). This transfer is consistent with our definition of snow; snow is the larger ice crystal class which is initiated only by vapor-grown pristine ice crystals. During ice subsaturated conditions, transfer of number concentration and mass mixing ratio from the snow category to pristine ice is conversely, calculated. The mean size of the pristine ice crystals are bounded by a size, D_b, which is set to 120 μm (this threshold size can be modified by the user). The mean size of pristine ice is not allowed to grow beyond this size while the snow mean size is not allowed to become less than D_b. Since, pristine ice and snow conform to the complete generalized gamma distribution functions both implicitly contain crystals of all sizes. Therefore, the transfer of crystals from pristine ice to snow is calculated by considering the change of mass mixing ratio and number concentration in the range $D_b \rightarrow \infty$ of the pristine ice distribution. Similarly, the snow transfer of mass mixing ratio and number concentration is calculated by considering the change in the region $0 \rightarrow D_b$ of the snow distribution. These equations were developed by Harrington et al. (1995) and summarized in Part I.

During subsaturated conditions, the mass mixing ratio that evaporates/sublimates from the water/ice classes is described by integrating the mass vapor depositional growth equation over the distributions as described in Part I. Physically it is expected that the smallest ice hydrometeors in the distribution will disappear completely into vapor in a given time-step. Therefore, a parameterization of number concentration loss due to evaporation/sublimation was formulated (Harrington et al., 1995). This is accomplished by considering the fractional number concentration loss (N_f) from the

distribution to be a strong function of the fractional mixing ratio lost (R_f) in a time-step, the distribution shape parameter (ν), and for pristine ice and snow categories, the crystal habit (H). The equation may be written as,

$$N_f = F_e(R_f, \nu, H),\qquad\qquad(2.18)$$

where

$$N_f = \frac{\Delta N_t}{N_t},\qquad\qquad(2.19)$$

and

$$R_f = \frac{\Delta r}{r}\qquad\qquad(2.20)$$

where r is the mass mixing ratio of a given species, N_t is the total number concentration of a given species, and ΔN_t is the change in number concentration due to evaporational/sublimational loss of a given species. Formulation of an analytical function, F_e, in (2.18), however, is non-trivial. Our solution is to calculate values of the fractional number concentration loss using a bin model representation of the distribution function, $n(D)$. In this bin model, an initial, normalized distribution was slowly evaporated in a subsaturated environment. During every time-step the mass loss from each bin is calculated, if the mass loss to evaporation/sublimation is greater than the mass in the bin then the crystals are assumed to have completely disappeared into vapor which constituted a number concentration sink. Fractional loss within each bin is also considered. By adding up the values of mass and number concentration lost to sublimation, tables can be created of N_f and R_f for a given ν and H. These tables were constructed for each category for number loss ratio for ranges of mass loss from 0.1 to 1.0, for prescribed values of ν, and for all crystal habits. This method was tested for pristine ice crystals and snow against variations in external parameters such as temperature, pressure, and ice saturation ratio. It was found by Harrington (1994) that these parameters have little effect on the tabulation of these ratios.

2.1.7. Melting and shedding

The ice distributions can be greatly modified depending on which type of melting and shedding physics is incorporated into the model. Melting is strongly affected by the relative humidity profile. Rasmussen and Heymsfield (1987b) stated that melting may not commence until 5 to 8°C in dry, evaporative conditions. Another problem concerned with melting is that during melting of low density graupel the particle completely soaks with water (Kidder and Carte, 1964; Prodi, 1970; and Rasmussen and Heymsfield, 1987a), effectively transforming the particle into a higher density hail particle which would lead to a conversion to the hail category. In melting regions, small stones should melt first leaving the larger stones. Lin et al. (1983) and Rutledge and Hobbs (1984) kept the intercept of the distribution constant during melting, but Orville and Kopp (1977) and Kopp et al. (1983) showed that this method produced unrealistically large decreases in the ratio of large to small particles and consequently lowered melting rates. Ferrier (1994) attempted a more realistic approach by melting the smallest ice particles completely within a time-step while assuming an exponential hydrometeor distribution.

His model produced the opposite effect to holding the intercept constant since many more of the smaller particles were removed from the distribution. This scheme resulted in unrealistically large mean particle diameters below the melting level with substantially smaller melting rates than in the constant intercept approach.

A more detailed description of the mass mixing ratio tendency due to melting used in RAMS can be found in Part I. Since pristine ice crystals are assumed to be all ice, any melted mass is converted to cloud water. A corresponding fraction of the number concentration of the crystal is assumed to be lost during melting. It is assumed that the snow and aggregate categories lose all melted mass during the melting process. This melted mass is converted to the graupel category along with an equal amount of ice mass from the snow or aggregate category. To determine the number concentration tendency lost by snow and aggregates, an explicit bin model was used similar to the technique used for evaporation (see Section 2.1.6). The results are expressed in terms of the fractional number concentration loss (N_f) from the distribution as a function of the fractional mixing ratio lost (R_f), the distribution shape parameter (ν), and for the snow category, the crystal habit (H). Number concentration and mixing ratio tendencies due to melting of graupel and hail is more complicated due to the mixed-phased capabilities of these species. Graupel is able to maintain a small percentage of liquid before converting to the hail category. Once the fraction of water in graupel reaches 30% the graupel spectrum is assumed to be transformed into a high density hail category. Since hail is assumed to be a mixed phase hydrometeor, a melt table is formulated to determine the number tendency of hail particles which completely melt into rain. This number concentration tendency is similar to the melt table for snow and aggregates. The conversion of mass from hail to rain is complicated by the additional process of shedding. These two processes are handled simultaneously in a look-up table to circumvent over-depletion by these two processes if handled separately. The mass tendency due to complete melting of the smallest hailstones to raindrops is handled similarly to the number concentration tendency for the same process. The impact of shedding on the mass tendency of hail and mass and number tendency of raindrops is discussed next.

Shedding from hail can produce a significant number of liquid particles which can be a significant source of rain and potential hail embryos. Lesins and List (1986) describe that the shedding process represents an instantaneous conversion of cloud to rain. Rasmussen and Heymsfield (1987c) also point out that the concentration of shed drops in a moderate up draft may be 10^3 times higher than the number of shedding hailstones. Hail must be large enough to shed liquid water with observations indicating that sizes (D) greater than 0.5 cm (Heymsfield and Hjelmfelt, 1984) to 0.8 cm are necessary (Rasmussen et al., 1984). Chong and Chen (1974) determined the critical amount of water carried by an ice core based on the radius of an ice core. Lesins and List (1986) observed 5 growth regimes and determined an ice fraction minimum to be 0.5. Rasmussen et al. (1984) observed much more water being retained than Chong and Chen (1974). They devised an expression for the critical mass of water on the ice core's surface before shedding occurs $(M_{W\text{crit}})$ dependent on the mass of the ice M_i,

$$M_{W\text{crit}}(D) = a + bM_i(D), \qquad (2.21)$$

where $a = 0.268 \times 10^{-3}$ kg and $b = 0.1389$. This shedding approach is used in RAMS. Any hydrometeor which has liquid water mass M_l exceeding M_{wcrit}, sheds that excess. The dependence of liquid and ice fraction on hail size before shedding depends on whether melting or accretion dominates. It is assumed that the melting process is responsible for liquid water accumulation in hail in order to determine how M_i and M_l depend on size before shedding. It should be noted that the melting process can include water that is soaked into the ice lattice and, therefore, is not available for shedding. It is not feasible at this point to treat this effect within a bulk microphysical framework and, thus, we approximate all melted water as a given bulk fraction of the total mixed-phase mass-mixing ratio. This liquid mass-fraction is the water that we assume is available for shedding.

Rasmussen and Heymsfield (1987a) stated that shedding is independent of altitude for non-tumbling hail. The size of the drops shed by hail and graupel are observed to be between 0.5 and 2.0 mm with a 1 mm modal size (Rasmussen et al., 1984b and Lesins et al., 1980). The mixing ratio of the mass shed by the ice spheres is calculated, and the number of raindrops shed is determined by assuming that the shed size is $D_{\text{shed}} = 0.001$ m,

$$N_{\text{shed}} = \left(\frac{r_{\text{shed}}}{\pi/6 D_{\text{shed}}^3} \right), \tag{2.22}$$

where r_{shed} is the mixing ratio of the rain shed, and D_{shed} is the size of the shed drops.

2.1.8. Sedimentation

In RAMS, transport of hydrometeors due to resolved and sub-grid air motions in the model is evaluated elsewhere (see Eq. (2.1)); sedimentation only deals with the mass-weighted relative fall velocity between the hydrometeor class and air, which is given by

$$\bar{v}_t = \alpha_{vt} D_n^{\beta_{vt}} \frac{\Gamma(\nu + \beta_{vt})}{\Gamma(\nu)}. \tag{2.23}$$

After evaluating Eq. (2.1) without the SEDIM(A) term, and updating mixing ratio r and concentration n based on all other terms, sedimentation is then carried out on the updated mixing ratios and number concentrations to obtain a final value for the time-step.

Following Part I, a Lagrangian scheme is used to transport the mixing ratio from any given grid cell to a lower height in the vertical column. In evaluating the SEDIM term for number concentration for each hydrometeor, it is assumed that N_t is transported in the same proportion as mixing ratio. This procedure ensures that the mixing ratio and number concentration of each hydrometeor does not fall into separate grid volumes due to sedimentation.

2.2. Equation closure

There is always the potential that in some situations the model may predict number concentrations and mixing ratios that are inconsistent with each other resulting in the

Table 4
Diameter bounds for each of the hydrometeors with $D_{n\min}$ and $D_{n\max}$

Hydrometeor	$D_{n\min}$ (m)	$D_{n\max}$ (m)
cloud droplets	1.0e-6	4.0e-5
rain	4.0e-5	0.01
pristine ice crystals	1.0e-6	1.2e-4
snow	1.2e-4	0.01
aggregates	1.0e-6	0.01
graupel	1.0e-6	0.005
hail	1.0e-6	0.01

diagnosis of extreme hydrometeor diameters. This is most likely along sharp boundaries of the cloud or precipitation shafts (Stevens et al., 1995). As a precaution, a check on the characteristic diameter of each hydrometeor category is made to make sure that the values are in bounds when the diameter is diagnosed in the two-moment scheme. If the diagnosed diameter is smaller than $D_{n\min}$ or larger than $D_{n\max}$, it is assumed that the diameter is out of bounds and the concentration is re-diagnosed based on that limiting diameter (see Table 4). Tests are performed in (see Section 3.2) to show how frequently this diameter readjustment is needed.

3. Model tests

In this section we show the results of the numerical simulations performed with RAMS and make comparisons of the two-moment prediction results with single-moment results similar to those presented in Part I. Sensitivity of the two-moment microphysical scheme of RAMS to selected parameters such as the shape parameter (ν), number concentration (N_t) of cloud droplets, and habit type are also tested and examined in this section. Comparisons are made only between simulations performed here; no attempt is made in this work to compare with results from previous model versions or with observations as this will be done in subsequent papers. As was the case in Part I, sensitivity tests are presented to demonstrate the versatility of the model and show how a few of the model-prescribed variables can produce dramatically different results.

3.1. Model setup

For simplicity, the model is configured similarly to Part I with a two-dimensional computational domain over flat terrain, with no surface fluxes of heat or moisture. A deep convective cell which produces large amounts of both liquid and ice is simulated. The computational domain is 24 km deep and 50 km in the horizontal extent, with grid spacing of 500 m in the horizontal and 300 m in the vertical. Initial conditions consist of zero winds, potential temperatures of 306 K and 218 K at the surface and 11 km, respectively, with a constant lapse rate between and a constant potential temperature above. The water vapor mixing ratio is set to 15.0 g kg^{-1} below 2 km and very dry

Table 5
Sensitivity tests and setup

Experiment	Moments	ν	N_c	Crystal habit
EXP1	2	1	300 cm^{-3}	hexagonal plates
EXP2	1 except for PI	1	300 cm^{-3}	hexagonal plates
EXP3	2	1	60 cm^{-3}	hexagonal plates
EXP4	2	1	1500 cm^{-3}	hexagonal plates
EXP5	2	3	300 cm^{-3}	hexagonal plates
EXP6	2	1	300 cm^{-3}	variable habits
EXP7	2	1	300 cm^{-3}	variable habit with vertical dependence

(0.01 g kg^{-1}) above 3 km. A Rayleigh friction absorbing layer is used above 18 km to prevent gravity wave reflection off of the rigid upper lid. Convection is initiated by a domain-centered bubble in the horizontal, 10 km wide and 3 km deep, with a temperature 5 K warmer and 2 g kg^{-1} moister than the environment. This simulation is quite explosive (2600 J kg^{-1}), and it is done purposely to exercise the microphysical scheme to a point which is near the physically-expected limits of a convective storm.

The sensitivity experiments are summarized in Table 5. These experiments test the sensitivity of the model to the one-moment scheme, and the parameters ν, N_t of cloud droplets, and the different pristine ice crystal and snow habit schemes in the model. All experiments assume pristine ice crystals and snow are hexagonal plates, except for Experiments 6 and 7. Two-moments are predicted in every experiment except EXP2 (where only pristine ice crystals have a two-moment prediction), and the cloud droplet number concentration (N_t) is set to 300 cm^{-3}, and $\nu = 1$ for all categories except in EXP5 $(\nu = 3)$.

Convection develops nearly identically in the first several minutes for all experiments. Buoyancy is dominated by the initial warm bubble in the first few minutes, and by latent heat release for several minutes afterward. Significant differences in most fields become readily apparent by 15 minutes, and these differences grow rapidly. Variations of microphysical fields across experiments due to different values of microphysical parameters strongly impact the convective motions, which, in turn, feed back upon the evolving microphysical fields. At 30 minutes into the simulations, convective scale motions are still present in all cases, but the kinematic fields have diverged significantly. A simulation time of 15 minutes was chosen to present and discuss some of the differences between the experiments since the differences are not a direct result of the kinematics at this time and precipitation was starting to reach the ground. The two-moment scheme adds nearly 15% to the time integration of the model relative to the one-moment scheme, however, code optimization is currently underway.

3.2. Model results

Some of the model fields from EXP1 are shown in Fig. 1. The cloud water field shows locally high amounts being injected into the updraft core (Fig. 1a), with peak values close to 5.0 g kg^{-1}. These peak cloud water mixing ratios highlight the relatively

slow conversion of cloud water to the ice categories in the main core of the updraft. The total mixing ratio field (Fig. 1b) shows very moist boundary layer air being transported into the middle-troposphere via the updraft core. The updraft peak velocities Fig. 1d approach 52 m s^{-1} with weaker updrafts situated away from the center of the grid on both sides initiated by gravity waves excited by the initial convective pulse. Fig. 2 shows the predicted hydrometeor mixing ratio fields for EXP1. Rain mixing ratio is displaced away from the storm center in secondary updrafts near 4 km AGL, with peak values of 2.5 g kg^{-1}. The rainwater which is produced in the updraft core is quickly converted to hail higher above the melting level due to collection processes. The low density ice categories are located high in the troposphere producing the anvil cloud. Glaciation is initiated by pristine ice crystals which are heterogeneously produced above 5 km AGL. These crystals grow by vapor deposition and convert to snow, which initiates the riming process, enabling larger crystals such as the aggregates, graupel and hail to be produced. In the presence of liquid water, most of this ice mass is converted to hail due to collection, and consequently, hail mixing ratios peak at nearly 6 g kg^{-1}. Pristine ice crystals dominate the anvil mass with peak values of 3 g kg^{-1}, nearly 5 times greater than snow and aggregate mixing ratio values. Later in the simulation, however, snow and aggregate mass dominate pristine ice crystal mass due to deposition and collection sources. Graupel mixing ratios are relatively small due to the high LWC in the storm which quickly converts much of the graupel mass over to the hail category.

The hydrometeor concentration fields shown in Fig. 3, exhibit peak rain number concentrations in the updraft core near 6 km (peak values of 2 l^{-1}) This is not co-located with maxima found in the rain mixing ratio fields. These high values of rain concentration found in the updraft core are produced by autoconversion of cloud droplets. Most of the 'large' raindrops in the updraft are quickly converted to hail as a result of hydrometeor collisions effectively transforming the mean of the distribution to smaller sizes (see Fig. 4a). The ice categories show a structure similar to their mixing ratio fields with peak number concentrations located in the upper troposphere. The pristine ice number concentrations peak values are 9.0×10^4 l^{-1} at temperatures colder than $-40°C$. These crystals are produced by homogeneous freezing of the entire cloud droplet and part of the haze population. This type of simple simulation may produce higher number concentrations due to weak ambient flow which minimizes the flux of the pristine ice crystals out of the region. Snow and aggregate concentrations in the anvil reach 500 and 100 l^{-1}, respectively, due to conversion of pristine ice crystals by vapor deposition and aggregation. Graupel and hail number concentrations peaked near 0.5 and 0.2 l^{-1}.

The two-moment prediction scheme diagnoses the hydrometeor mean diameter, and these are shown in Fig. 4. These diameters are the mean diameters of the hydrometeor distribution in a bulk microphysical sense and should be understood in this context. The rain field shows diameters ranging from 0.3 mm to 1.5 mm, with the largest mean raindrop diameters found near 4 km AGL, 5 km on either side of the domain center. This is a prime location for long residence times for rain since it is just below a cloud droplet source region, and other ice categories do not exist here which minimizes the potential sink due to collection. Pristine ice crystals, snow, and aggregates exist primarily in the upper regions of the cloud. The sizes of these low density ice categories
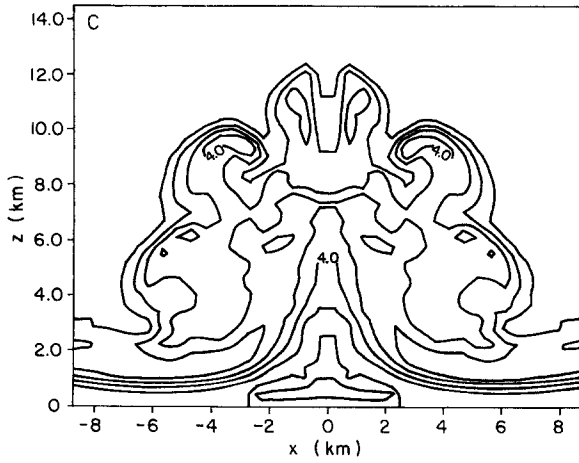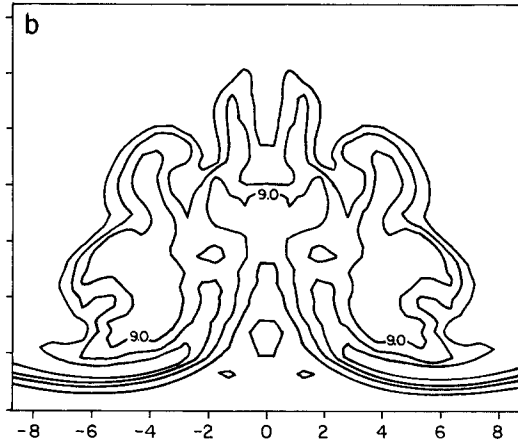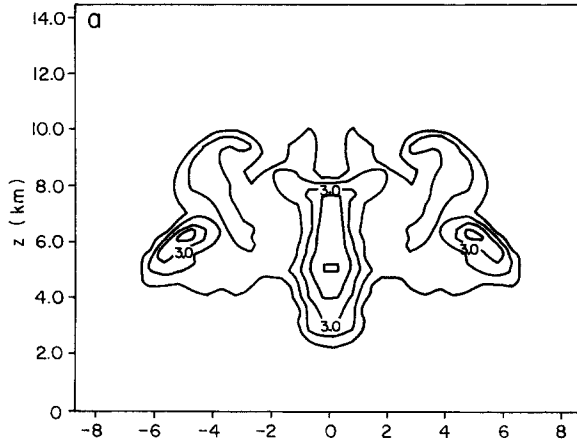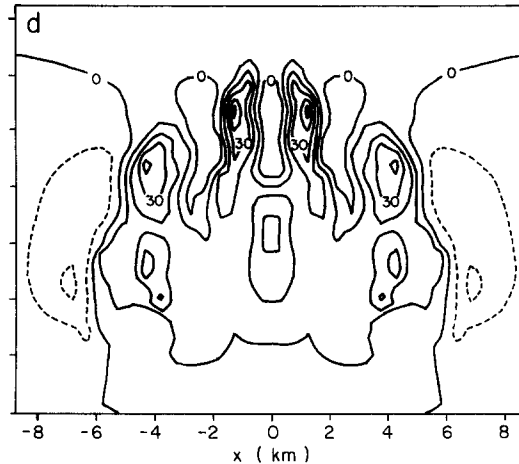
Fig. 1. EXP1 simulated fields at 15 minutes. Contour intervals and maxima are shown in brackets. These and subsequent figures are 'windowed in' to focus on the area of interest: (a) r_c [1.0 g kg^{-1}, 5.0 g kg^{-1}], (b) r_t [3.0 g kg^{-1}, 15.0 g kg^{-1}], (c) N_{in} [1 × 10^4 m^{-3}, 6 × 10^5 m^{-3}], (d) w [10.0 m s^{-1}, 50.0 m s^{-1}].

are especially small due to the small LWC found high in the cloud. These crystals do exist at lower altitudes, but they are quickly collected by rain and converted to hail in these regions. Most of the pristine ice crystal diameters are near 10 μm and the mean diameter of snow is near 100 μm. The mean diameters of aggregates and graupel are a bit larger with peak sizes near 1.0 mm. The hail category exists over a broad range of sizes with large diameters found near the center of the grid. The maximum mean diameters of hail are nearly 2.5 mm. The mean diameter of hail is smaller than would be expected for 'observable' hail but the hail category in RAMS also takes into account frozen drops, which will tend to weight the distribution towards smaller sizes. Also, since a gamma distribution is assumed, hail diameters much greater than the mean diameter exist. One question raised in Section 2.2 was the importance of closing the physics with $D_{n\text{min}}$ and $D_{n\text{max}}$. A check to determine the amount of time these limits were exceeded showed that it occurred less than 5% of the time which is very acceptable. The bounds were exceeded usually in tight gradient regions of the cloud where mixing ratios were low, and evaporation was taking place.

The mixing ratio fields from EXP2 are shown in Fig. 5. This experiment predicts one moment of each hydrometeor category (except two-moments for pristine ice crystals), the mixing ratio, and assumes a fixed mean diameter for each species. The mean particle mass has a diameter of 0.1 cm for rain, snow, and aggregates, 0.3 cm for graupel, and 0.5 for hail. The rain mixing ratio category (Fig. 5a) exhibits a more widespread structure from the EXP1, with rain mixing ratio values greater than 1.0 g kg^{-1} extending up to 8 km AGL. The low density ice categories show pristine ice mixing ratios nearly a 1.0 g kg^{-1} greater than EXP1 run, but this surplus is at the expense of snow, aggregate and graupel categories which are much less than found in EXP1. With the constraint of specifying the mean diameter of the hydrometeor category, the one-moment scheme effectively limits the amount of snow, aggregates and graupel. The
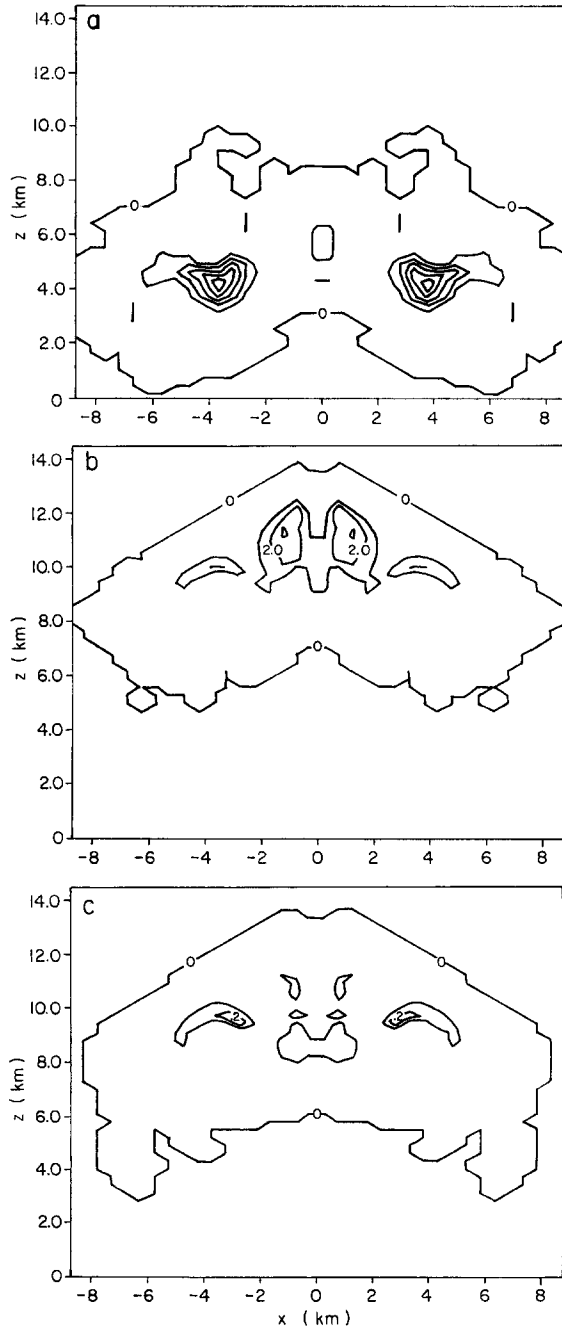
Fig. 2. EXP1 microphysical fields at 15 minutes. Contour intervals and maxima are shown in brackets. Units are [g kg^{-1}] for mixing ratios: (a) r_r [0.5, 2.5], (b) r_p [1.0, 3.0], r_s [0.1, 0.3], (d) r_a [0.1, 0.4], (e) r_g [0.05, 0.1], (f) r_h [1.0, 6.0].
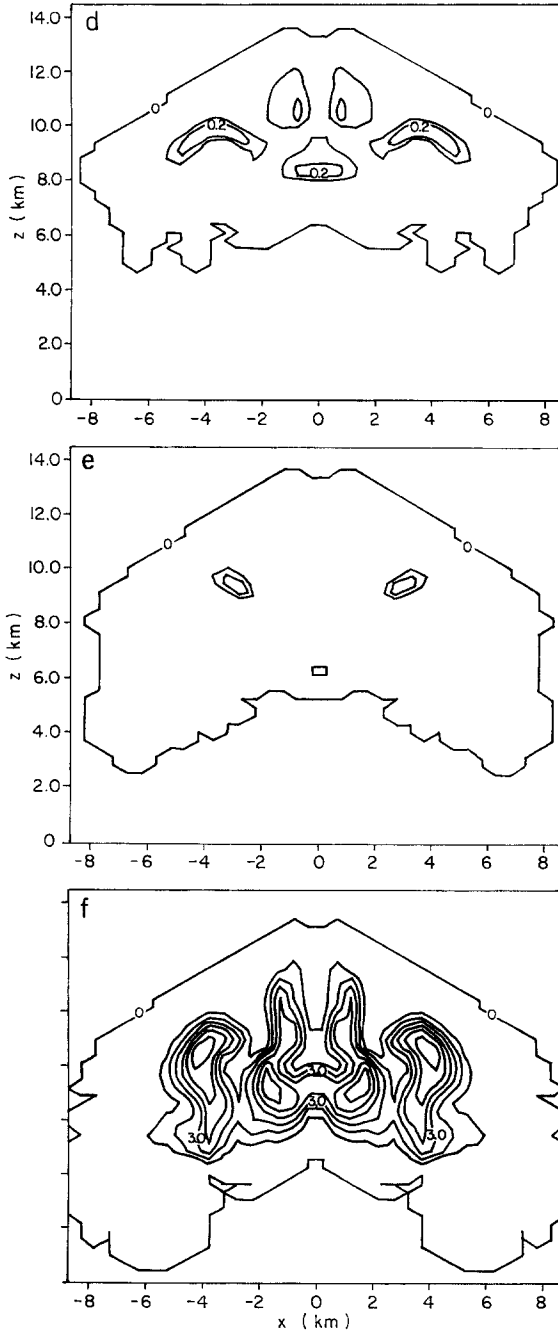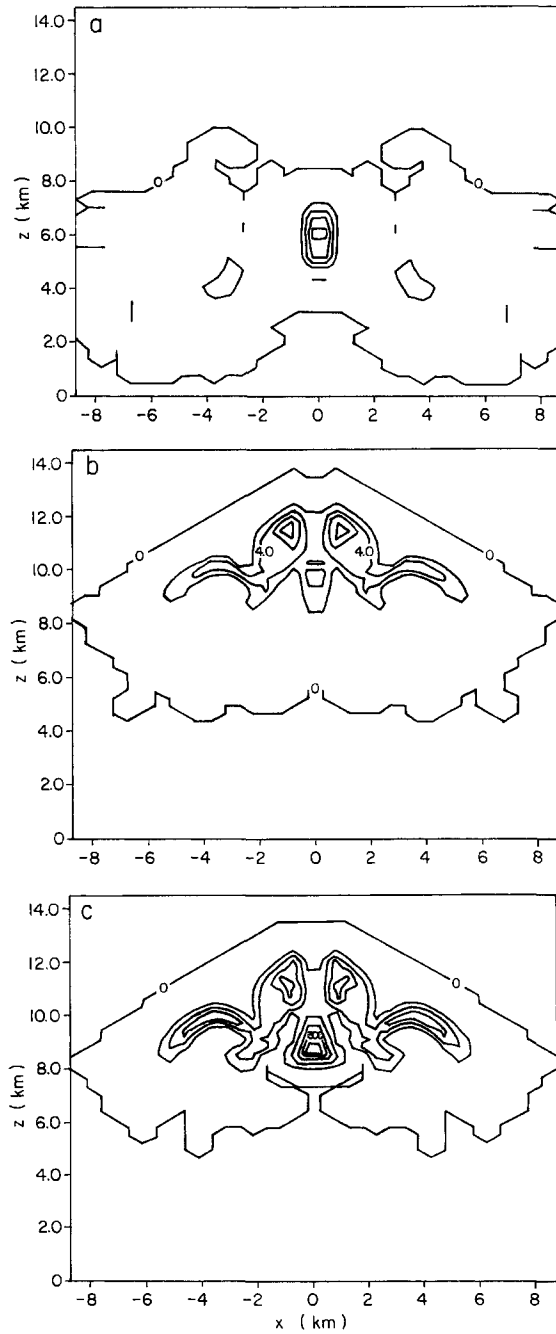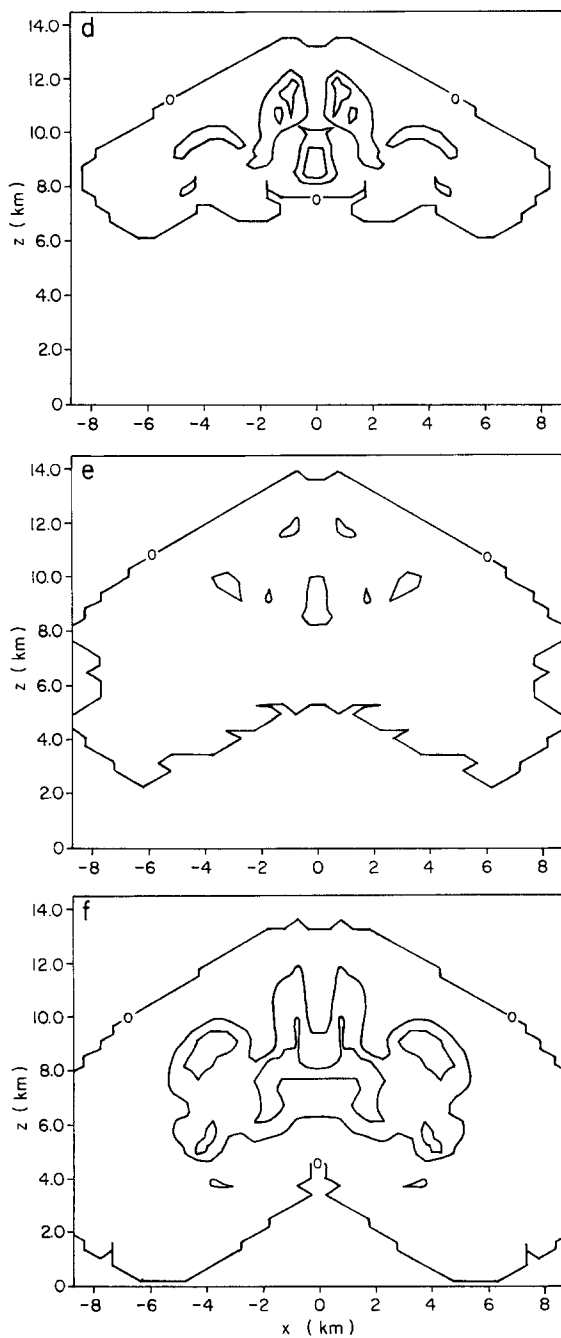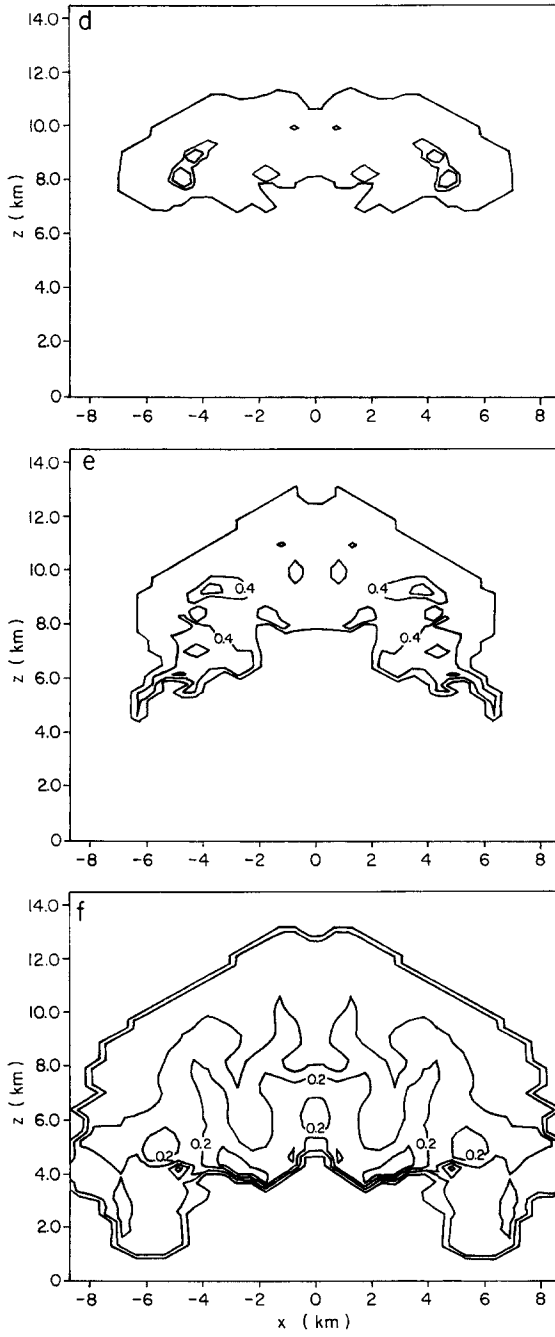
Fig. 2 (continued).

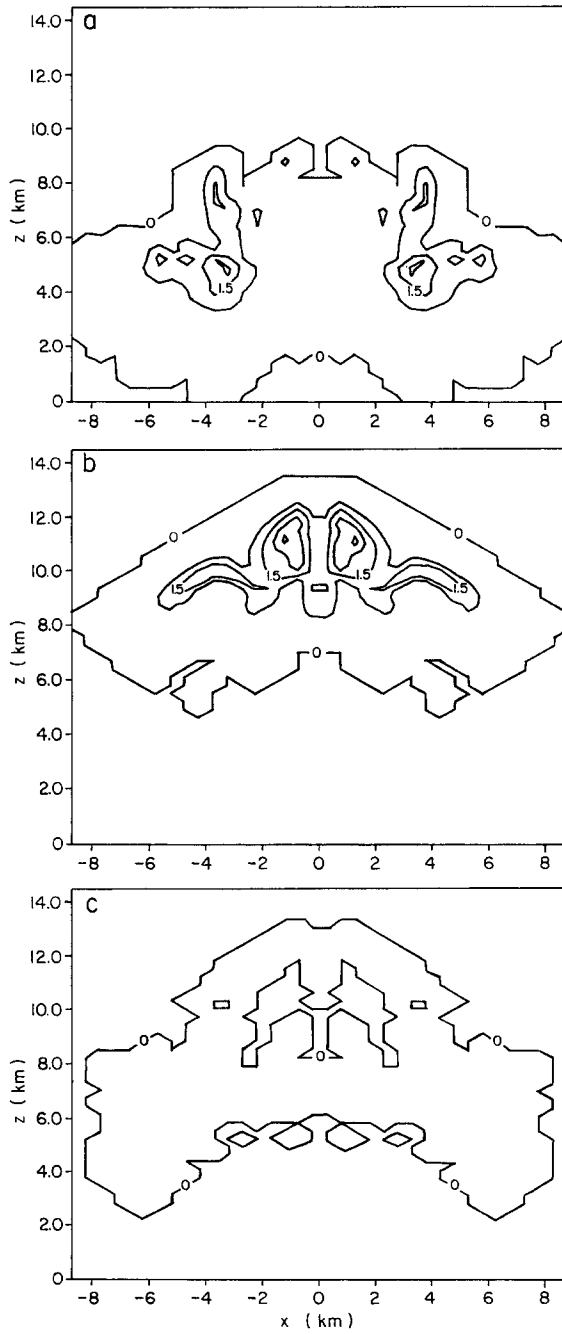Fig. 3. EXP1 microphysical fields at 15 minutes. Contour intervals and maxima are shown in brackets. Units are $[l^{-1}]$ for concentrations: (a) n_r [0.5, 2.0], (b) n_p [2.0×10^4, 8.0×10^4], (c) n_s [100.0, 500.0], (d) n_a [50.0, 100.0], (e) n_g [0.5, 0.5], (f) n_h [0.1, 0.2].

Fig. 3 (continued).
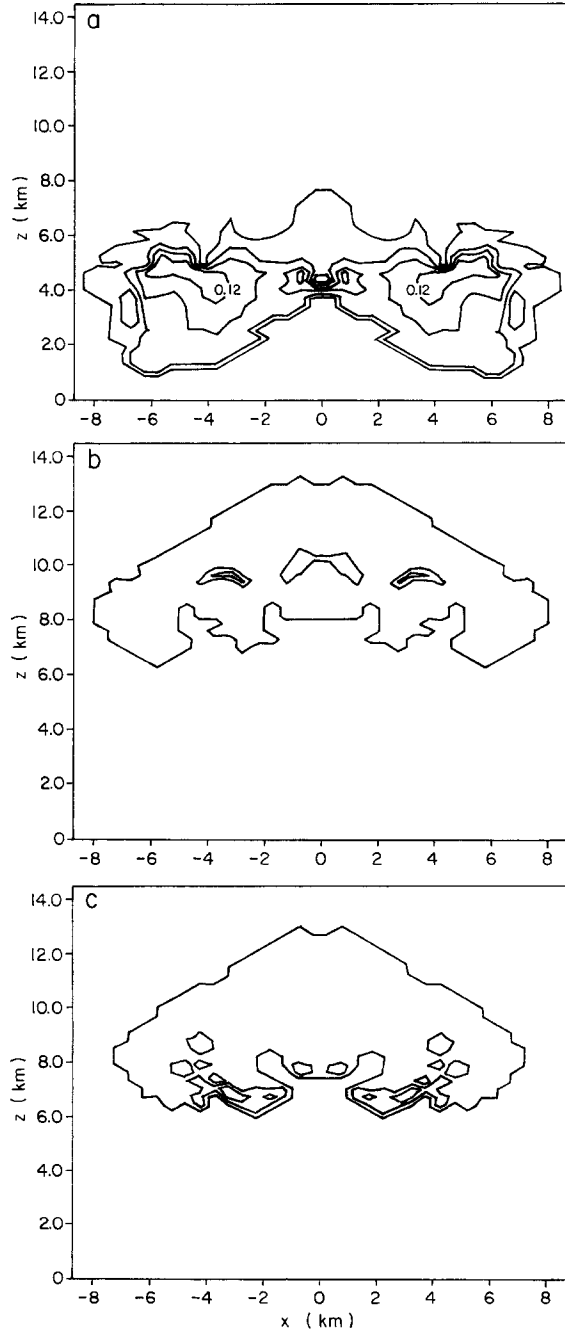
Fig. 4. EXP1 microphysical fields at 15 minutes. Minima, contour intervals, and maxima are shown in brackets. Units are diameter in [m]: (a) d_r [0.3×10^{-3}, 0.3×10^{-3}, 0.15×10^{-2}], (b) d_p [0.1×10^{-4}, 0.2×10^{-4}, 0.5×10^{-4}], (c) d_s [0.6×10^{-4}, 0.6×10^{-4}, 0.18×10^{-3}], (d) d_a [0.2×10^{-3}, 0.2×10^{-3}, 0.1×10^{-2}], (e) d_g [0.2×10^{-3}, 0.2×10^{-3}, 0.8×10^{-3}], (f) d_h [0.5×10^{-3}, 0.5×10^{-3}, 0.25×10^{-2}].

Fig. 4 (continued).

Fig. 5. EXP2 microphysical fields at 15 minutes. Minima, contour intervals, and maxima are shown in brackets. Units are [g kg^{-1}] for mixing ratios: (a) r_r [0.5, 1.0, 2.5], (b) r_p [0.5, 1.0, 3.5], (c) r_s [0.05, 0.05, 0.05], (d) r_a [0.05, 0.1, 0.35], (e) r_g [0.05, 0.05, 0.05], r_h [1.0, 1.0, 7.0].
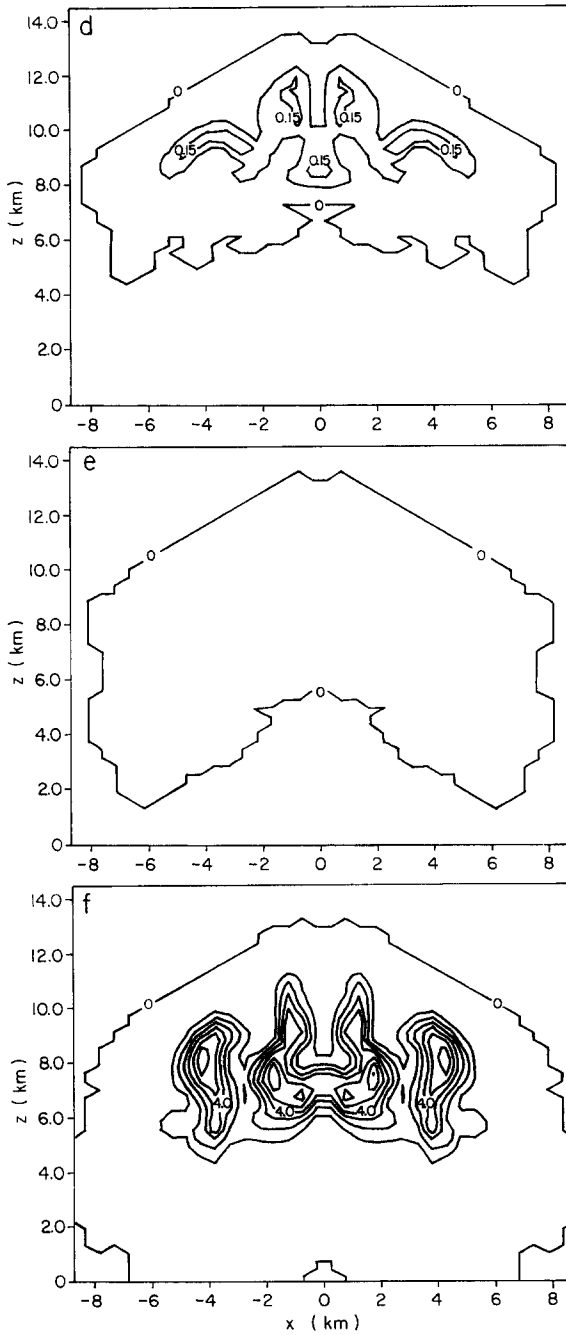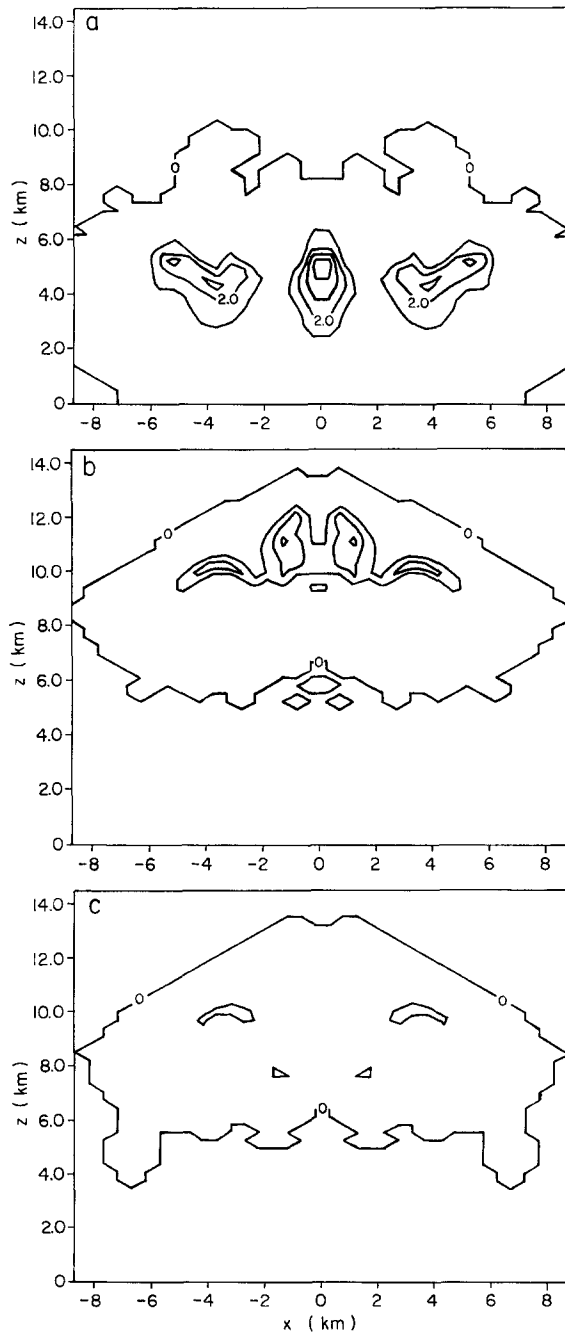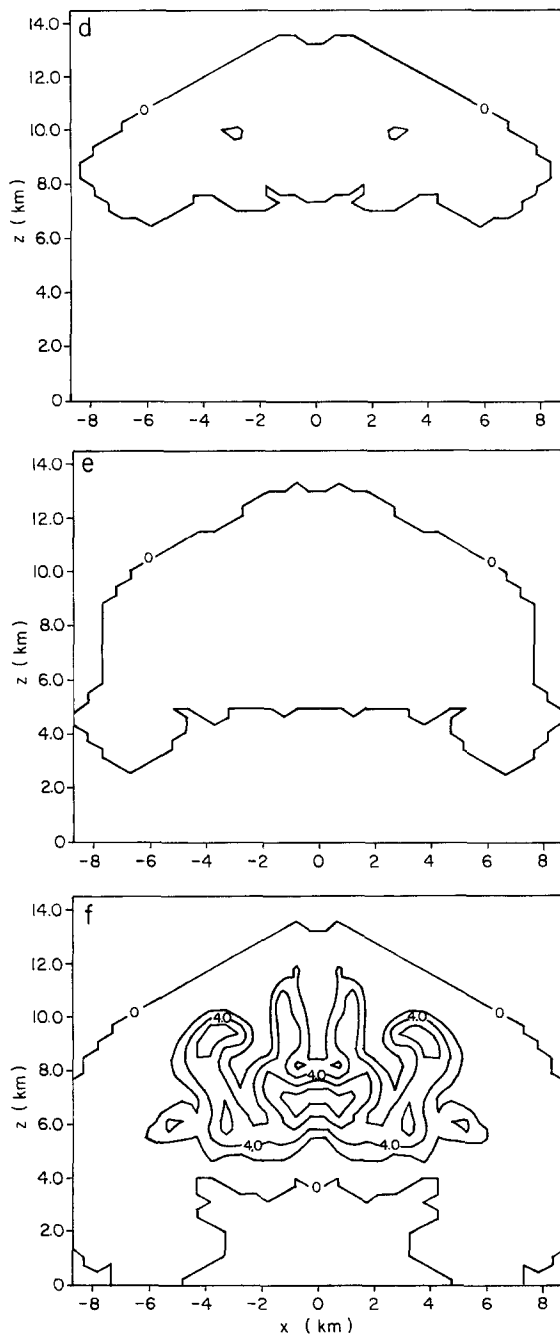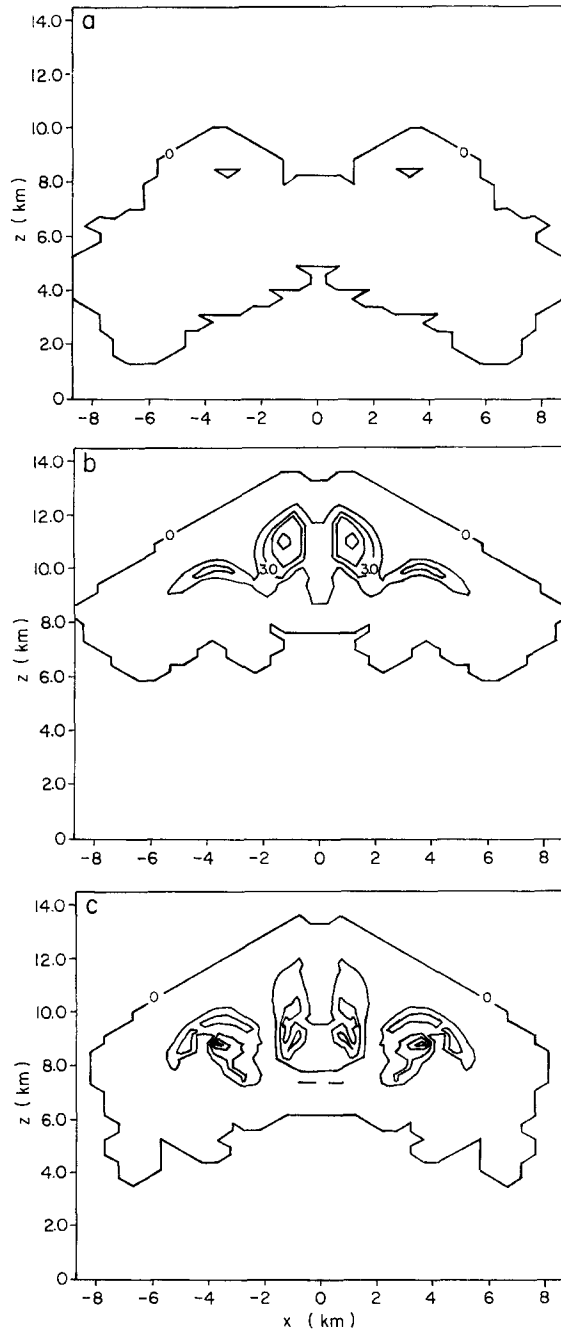
Fig. 5 (continued).

Fig. 6. EXP3 microphysical fields at 15 minutes. Contour intervals and maxima are shown in brackets. Units are [g kg^{-1}] for mixing ratios: (a) r_r [1.0, 5.0], (b) r_p [0.5, 1.5], r_s [0.05, 0.05], (d) r_a [0.05, 0.05], (e) r_g [0.05, < 0.05], (f) r_h [2.0, 8.0].

Fig. 6 (continued).

Fig. 7. EXP4 microphysical fields at 15 minutes. Contour intervals and maxima are shown in brackets. Units are [g kg^{-1}] for mixing ratios: (a) r_r [0.5, < 0.5], (b) r_p [1.5, 7.0], (c) r_s [0.15, 0.9], (d) r_a [1.0, 3.0], (e) r_g [0.5, 3.5], (f) r_h [1.0, 2.0]. Note the different contour intervals for r_a and r_g from previous figures.
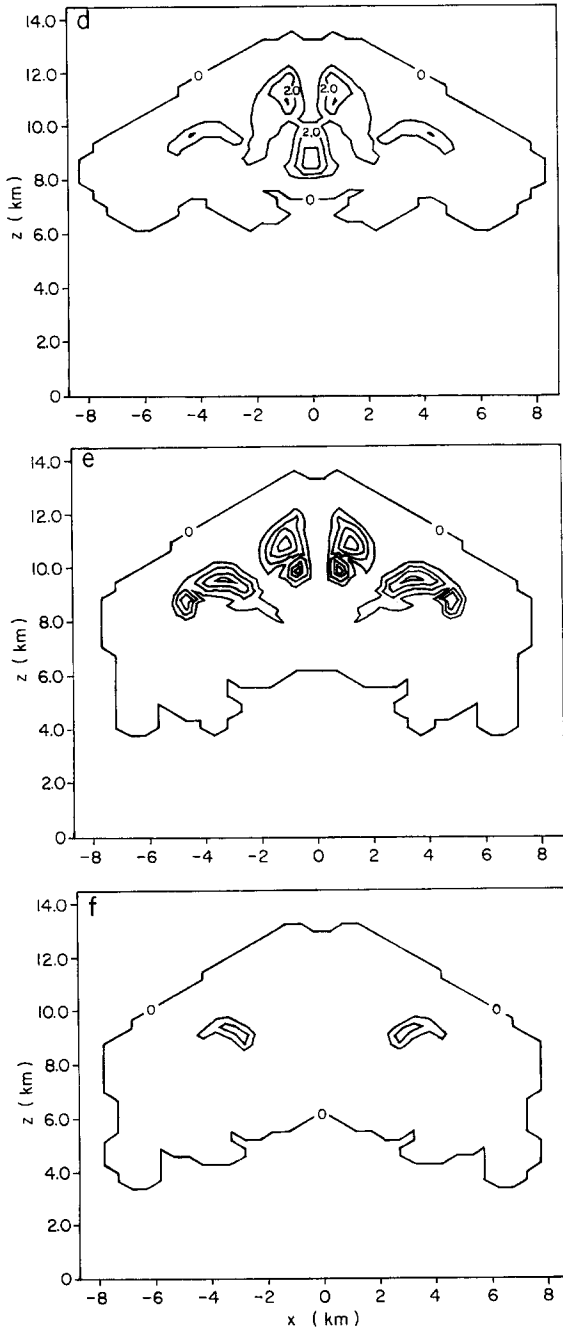
Fig. 7 (continued).

prescribed diameters of these categories are relatively large, which decreases the residence time in regions in the presence of liquid water due to enhanced collection efficiencies and conversion to hail. As a consequence, rain extends to higher altitudes in this simulation than EXP1 due to the lack of ice hydrometeors at the 5–8 km AGL level. Hail mixing ratios are relatively unchanged from EXP1.

EXP3 is the same as the EXP1 except that N_t of the cloud droplets is decreased to 60 cm^{-3} in an attempt to simulate clean maritime conditions. This effectively increases the auto-conversion of cloud water to rain as compared to the EXP1 which is exhibited by the decrease of 4 g kg^{-1} in the cloud water mixing ratio field (peak values near 1 g kg^{-1}). As evidenced by the mixing ratio fields (Fig. 6), significantly more rain mass is produced in the center of the domain by autoconversion of cloud droplets to rain (peak value 5 g kg^{-1}) in a location where relatively low amounts were found in EXP1. Significantly less low density ice mass is found at higher altitudes in the storm due to the greater amounts of rain mass being produced lower in the domain. Peak pristine ice crystal mixing ratios are 1.5 g kg^{-1}; nearly half that produced in EXP1. Snow, aggregate, and graupel mass display only negligible amounts. Hail, on the other hand, is produced more efficiently with the increased collection kernel of rain. Peak values of hail mixing ratio are nearly 9 g kg^{-1}. The number concentrations for the hydrometeors (not shown) exhibit much higher values for rain and hail (7 1^{-1} and 4.5 1^{-1}, respectively) and much lower values for snow, aggregates, and graupel as compared to the control run.

EXP4 is identical to the EXP1 except that N_t of cloud droplets is increased to 1500 cm^{-3}, consistent with very polluted continental air. The cloud water mixing ratio field is slightly greater than 8 g kg^{-3}, nearly 3 g kg^{-3} more than the EXP1. Fig. 7 shows the mixing ratio fields for EXP4. Since the cloud droplet concentrations are increased, the droplet diameter is reduced, resulting in a shut-down of warm rain processes, as evidenced by negligible rain mixing ratios. Later in the simulation, more significant rain mass is produced by the melting of the ice categories. All the low density categories, however, have increased dramatically. Pristine ice mass is up to 7.0 g kg^{-1} with snow and graupel increasing 300% (peak values 1.0 g kg^{-3} and 3.9 g kg^{-3} respectively). With negligible rain mixing ratios, conversion processes to hail are severely limited, resulting in peak hail mixing ratio values of 2.0 g kg^{-3}. The primary source for hail in this simulation is riming of graupel. The number concentrations of the low density categories increase similarly to the mixing ratio field, and the concentrations of the hail category have increased compared to EXP1. Most of this increase in the hail number concentration is due to collection of cloud water by the graupel particles and conversion to hail which results in smaller hail diameters than in EXP1.

EXP5 is identical to EXP1 except that breadth parameter of the distribution is increased from one to three for each hydrometeor. The cloud water mixing ratio (not shown) is much less than EXP1 with peak values near 0.5 g kg^{-1}. Rain mixing ratios (Fig. 8a) are dramatically higher with peak values near 7 g kg^{-1} and the rain structure shows highest values near the center of the grid where only low rain mixing ratios were found in EXP1. The increased rain mixing ratios are due to the increase in ν which increased the mean diameter of cloud water. This, in turn, sharply increases the autoconversion to rain. With so much rain mass occupying the lower troposphere, much
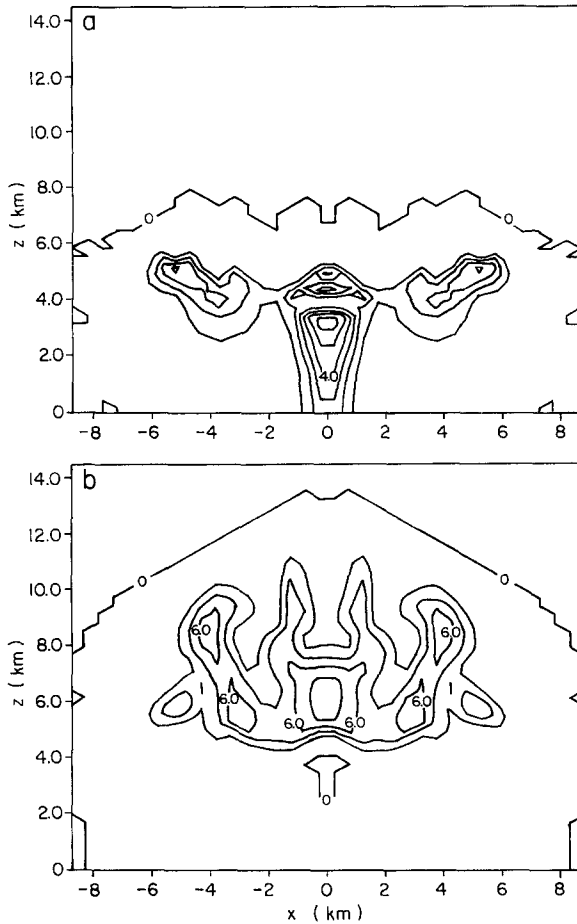
Fig. 8. EXP5 microphysical fields at 15 minutes. Contour intervals and maxima are shown in brackets. Units are [g kg^{-1}] for mixing ratios: (a) r_r [1.0, 6.0], (b) r_h [2.0, 8.0].

less low density ice mass is produced higher in the cloud. Most of the low density crystals are quickly collected by rain and converted to hail. Hail mass (Fig. 8b), as a result, is nearly 3.0 g kg^{-1} greater than EXP1. Many more raindrops are produced in EXP5 with peak values nearly 30 1^{-1}. Pristine ice crystals concentrations are nearly the same as the EXP1, however, snow and aggregate number concentrations are negligible. Graupel concentrations are much higher than in the EXP1, with peak values 72 1^{-1}. Hail concentrations are smaller than for EXP1 with peak values near 0.2 1^{-1}.

EXP6 shows a profound sensitivity to variable habit diagnosis in the model as described in Section 2.1.2. Much less pristine ice mass compared to the EXP1 exists in the upper cloud levels where the habits of the crystals are dominated by rosettes and needles. Another dramatic difference between the two runs is the increase in the graupel category. Graupel mass peaks at 1.8 g kg^{-1} which is much greater than in EXP1. The

Table 6
Maximum mixing ratios (g kg^{-1}) for sensitivity tests

Experiment	r_c	r_r	r_p	r_s	r_a	r_g	r_h
EXP1	5.0	2.5	3.0	0.35	0.4	0.1	6.0
EXP2	5.0	2.5	3.5	0.05	0.35	0.05	7.0
EXP3	1.0	5.0	1.5	0.05	0.05	0.05	9.0
EXP4	8.5	0.5	7.0	1.0	3.0	3.9	2.0
EXP5	0.5	6.0	0.5	0.0	0.05	0.05	9.0
EXP6	5.0	2.5	1.5	0.4	0.5	1.8	7.0
EXP7	5.0	2.5	1.5	0.4	0.5	1.5	7.0

reason for this increase is due to the dependence of the riming conversion process on habit. The habit of the crystal in EXP1 was a hexagonal plate which does not convert to graupel as easily as the columns and needles that prevail in this sensitivity experiment. The number concentrations for each of these categories are dramatically different than EXP1. Pristine ice crystal concentrations are nearly half that found in the EXP1, however, the number concentrations of snow, aggregates and graupel are significantly increased (2100 l^{-1}, 400 l^{-1}, and 950 l^{-1} respectively). Hail is much higher with peak values near 1.4 l^{-1}. EXP7 which utilizes the vertical dependent variable habit diagnosis as described in Section 2.1.2 shows only slight differences to EXP6. Slight increases in the number concentrations of pristine ice crystals and snow are found in EXP7. Slight decreases are found in the graupel concentrations as compared to EXP6. The overall mass fields are unaffected.

3.3. Discussion

These experiments show the sensitivity of the model to the user-specified input parameters for an idealized cumulus cloud initialized with a hot bubble. A summary of the maximum mixing ratios and concentrations from the sensitivity tests are shown in Tables 6 and 7. First, the tables highlight the high sensitivity of the model to the number of moments which are predicted. The overall maximum mixing ratio field shows more mass going into hail at the expense of the snow, aggregates, and graupel categories. This result is a consequence of the smaller diagnosed diameters in the two-moment predictive scheme (Fig. 4). Another striking feature is the spatial variability of the structure of the

Table 7
Maximum concentrations (l^{-1}) for sensitivity tests

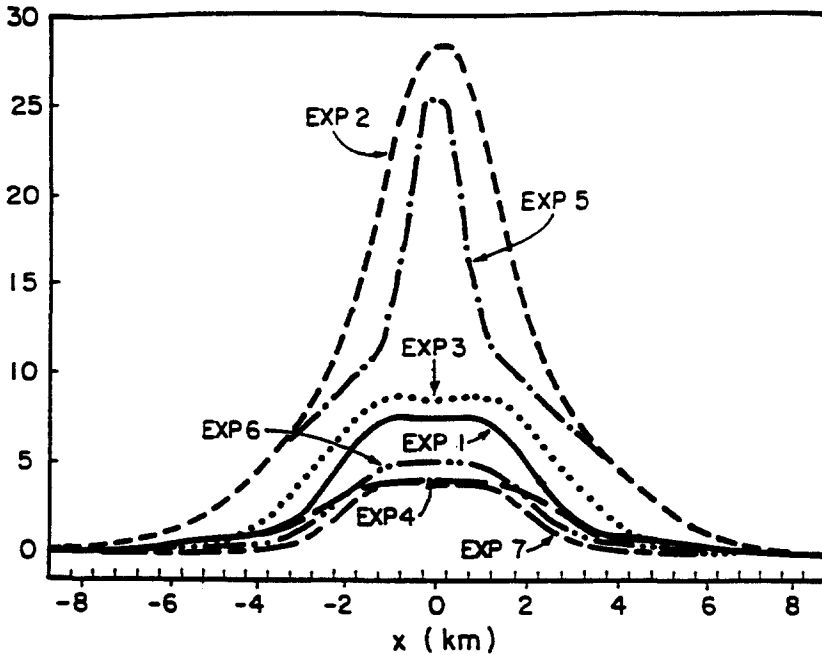| Experiment	n_r	n_p	n_s	n_a	n_g	n_h
EXP1	2.0	9×10^4	500	100	0.5	0.2
EXP3	7.5	9×10^4	300	50	0.05	2.3
EXP4	0.0	9×10^4	900	300	24	3.1
EXP5	30.0	9×10^4	0.0	0.0	72.0	0.2
EXP6	2.0	4×10^4	2100	400	950	1.4
EXP7	2.0	6×10^4	2300	400	850	1.5

Fig. 9. Accumulated precipitation after 30 minutes for each of the sensitivity runs. Units are in mm.

mean diameter field across the domain. The diameters are fixed in the one moment scheme, therefore the diameter cannot be adjusted by the varying microphysical conditions. The greatest difference between EXP1 and EXP2 is in the precipitation distribution (Fig. 9). Coincident with the relatively larger diameters in EXP2, precipitation amounts are nearly four times higher in EXP2 than found in EXP1. Nearly 70% of this precipitation falls in the form of hail (note that hail may be a mixed phased hydrometeor). The smaller hydrometeor diameters produced in EXP1 result in cloud precipitation processes which are less efficient, and more hydrometeor mass is injected into the upper regions of the cloud. The diameters and the resultant terminal velocities in EXP2 are fixed to very high values which enhances precipitation collection and fallout.

The set of experiments which modified the cloud droplet number concentrations (EXP3 and EXP4) had a large influence on the resultant microphysical fields. These tests, which basically investigated the sensitivity of warm rain processes, showed how important the auto-conversion of cloud droplets to rain was to the initiation of hydrometeor development in the middle troposphere in these environmental conditions. In EXP3, where the cloud droplet concentration was set to 60 cm^{-3}, the rain field was nearly doubled compared to EXP1. Consequently, hydrometeor collection of the smaller ice categories dramatically increased. This feedback resulted in much more hail mass being produced due to collection of the lower density ice crystals by rain in EXP3, decreasing low density ice mass amounts in the anvil region of the cloud. Interestingly, however, precipitation amounts increased only slightly in EXP3 over EXP1 (Fig. 9).

This slight increase was due to the smaller hydrometeor diameters found in EXP3. Even though much more hail mass was produced by collection, the interacting hydrometeors were relatively small snow, aggregate, and graupel particles. These collections resulted in a smaller collected hail category as compared to EXP1. With smaller sizes, precipitation efficiencies were decreased, but since more mass was converted over to hail in EXP3, more precipitation was produced. Warm rain processes were effectively eliminated, with the cloud droplet concentration set to 1500 cm^{-3}. Therefore, much more cloud water remained and was made available for the low density ice categories, with most of the mass being injected into the anvil. Hail mixing ratios were nearly one-third of EXP1. Precipitation efficiencies were drastically reduced and the total precipitation produced in this experiment was the lowest.

One problem with the breadth parameter is that there are not many observations of hydrometeor size distributions. Also, the exponential assumption, which is used widely by modelers, may not be correct in many situations. These experiments show that the microphysical structure is very sensitive to different values of ν. First, warm rain processes are more efficient with a higher specified ν of cloud droplets since the mean diameter of cloud droplets is increased by nearly 40% (Part I) which enhances the autoconversion of cloud droplets to rain. The increased collection kernel of rain collects much more snow, aggregate, and graupel mass (with a ν of 3 for all variables the collection kernel of these categories are also increased), and this collection results in more hail mass produced lower in the cloud. With an increased collection kernel of snow, aggregates and cloud droplets, and in the absence of rain, more conversion to graupel occurs higher in the cloud resulting in much higher graupel concentrations near 10 km AGL. Increasing ν also has a profound impact on the precipitation processes of the simulated cloud (Fig. 9). In EXP5, precipitation is more than three times greater than in EXP1, due to the increased diameters of the hydrometeors. However, less than 10% of the precipitation falls in the form of hail, as opposed to EXP2 where nearly 70% of the precipitation is in the form of hail. Rain precipitation dominates the total precipitation in EXP5 since much more rain is produced at lower altitudes and these droplets are larger in size.

The final sensitivity tests investigated the role of diagnosing the crystal habit on the microphysical structure of the cloud. As opposed to EXP1, EXP6 allows for variable habit diagnosis. The greatest impact of habit diagnosis in this convective environment is seen in the upper cloud region. The pristine ice crystals growth rates for needles, columns and rosettes are much greater than for hexagonal plates, and therefore more mass and number is converted to the snow categories in EXP6. EXP6 shows pristine ice crystal mixing ratios and number concentrations are nearly half those found in EXP1 due to conversion to the snow category. With more snow and aggregates available, more conversion to graupel due to riming is facilitated by the columnar crystals in this region. Therefore, graupel masses and number concentrations are much greater in EXP6 than EXP1. The sensitivity of changing the habit diagnosis based on a vertical dependence (EXP7) shows little change from EXP6. Precipitation amounts for EXP6 and 7 are slightly less than EXP1 (Fig. 9), possible due to more mass being partitioned to the anvil.

4. Conclusion

A two-moment hydrometeor prediction scheme has been implemented into RAMS. This development includes physics based on the most recent observations and parameterizations. The scheme predicts the mixing ratio and number concentration of rain, pristine ice crystals, snow, aggregates, graupel, and hail. Since two moments are predicted in the new scheme, it provides a better capability for remote sensing comparisons (such as multiparameter radar) by the model than a one-moment scheme.

Preliminary tests in an idealized convective environment showed that the two-moment scheme allows more freedom on the size distribution by predicting on both mixing ratio and concentration of each hydrometeor and allowing the mean diameter to evolve more realistically unlike the one-moment scheme. Modelers, however, need to recognize the potential sensitivity of some of these input parameters on the evolution of cloud processes in a simulated storm. Parameters such as cloud droplet concentrations are usually measured during field programs and have a good climatological database. These values should be understood for a given case environment due to the strong sensitivity of the model to this parameter. The shape of the size distribution ν, however, is not easily applied by modelers since these measurements are not typically conducted for various types of weather phenomena. More recent field projects such as WISP and FIRE, have specifically looked at the size distribution where the breadth of the distribution can be inferred, but many more measurements are needed. This argument is reinforced by the sensitivity of the simulated cloud structure to the ν parameter.

The modeling results also indicated some of the problems with not predicting on the aerosol and cloud droplet spectra. First, prediction of aerosols and cloud condensation nuclei (CCN) would allow for a more realistic prediction of the cloud droplet spectra. This prediction would impact warm rain auto conversion processes and collection of cloud water. Another implication for predicting on the aerosol and CCN populations would be with the homogeneous nucleation of cloud water and haze particles. Currently, this parameterization assumes fixed concentrations of cloud droplets and haze particles which may lead to over-prediction of pristine ice crystals produced by homogeneous freezing mechanisms. Since there is, in essence, a sustained supply of these freezing sites. A more explicit prediction of their concentrations should allow a more realistic simulation.

References

Berry, E.X., Reinhardt, R.L., 1974a. Analysis of cloud drop growth by collection. Part I: Double distributions. J. Atmos. Sci. 31, 1814–1824.

Berry, E.X., Reinhardt, R.L., 1974b. Analysis of cloud drop growth by collection. Part II: Single initial distributions. J. Atmos. Sci. 31, 1825–1831.

Brazier-Smith, P., Jennings, S., Latham, J., 1973. Raindrop interactions and rainfall rates within clouds. Quart. J. Roy Meteor. Soc. 99, 260–272.

Chong, S., Chen, C., 1974. Water shells on ice pellets and hailstones. J. Atmos. Sci. 31, 1384–1391.

Cotton, W.R., Stephens, M.A., Nehrkorn, T., Tripoli, G.J., 1982. The Colorado State University three-dimensional cloud/mesoscale model. Part II: An ice phase parameterization. J. Rech. Atmos. 16, 295–319.

Cotton, W.R., Tripoli, G., Rauber, R.M., Mulvihill, E.A., 1986. Numerical simulation of the effects of varying ice crystal nucleation rates and aggregation processes on orographic snowfall. J. Climate Appl. Meteor. 25, 1658–1680.

DeMott, P.J., Meyers, M.P., Cotton, W.R., 1994. Parameterization and impact of ice initiation processes relevant to numerical model simulations of cirrus clouds. J. Atmos. Sci. 51, 77–90.

Feingold, G., Tzivion, S., Levin, Z., 1988. Evolution of raindrop spectra. Part I: Solution to the stochastic collection/breakup equation using the method of moments. J. Atmos. Sci. 45, 3387–3399.

Feingold, G., Stevens, B., Cotton, W., Walko, R., 1994. An explicit cloud microphysics/LES model designed to simulate the Twomey effect. Atmos. Res. 33, 207–233.

Ferrier, B.S., 1994. A double-moment multiple-phase four class bulk ice scheme. Part I: Description. J. Atmos. Sci. 51, 249–280.

Gordon, G.L. and Marwitz, J.D., 1981. Secondary ice crystal production in stable orographic clouds over the sierra nevada. In: Eighth Conf. on Inadvertent and Planned Weather Modification, Amer. Meteor. Soc., 62–63.

Hall, W., 1980. A detailed microphysical model within a two-dimensional dynamical framework: Model description and preliminary results. J. Atmos. Sci. 37, 2486–2507.

Hallet, J., Mossop, S.C., 1974. Production of secondary ice particles during the riming process. Nature 249, 26–28.

Harrington, J.L., 1994. Parameterization of ice crystal conversion processes in cirrus clouds using double-moment basis functions. Master's thesis, Department of Atmospheric Science, Fort Collins, CO 80523. Atmospheric Science Paper No. 554.

Harrington, J.Y., Meyers, M.P., Walko, R.L., Cotton, W.R., 1995. Parameterization of ice crystal conversion processes in cirrus clouds using double-moment basis functions. Part I: Basic formulation and one-dimensional tests. J. Atmos. Sci. 52, 4344–4366.

Heymsfield, A.J., Hjelmfelt, M., 1984. Processes of hydrometeor development in Oklahoma convective clouds. J. Atmos. Sci. 41, 2811–2835.

Kessler, III, E., 1969. On the distribution and continuity of water substance in atmospheric circulation. Meterol. Monogr., Am. Meteorol. Soc., 84 pp.

Kidder, R., Carte, A., 1964. Structures of artificial hailstones. J. Rech. Atmos. 1, 169–181.

Kogan, Y., 1991. The simulation of a convective cloud in a 3-D model with explicit microphysics. Part I: Model description and sensitivity experiments. J. Atmos. Sci. 48, 1160–1189.

Kopp, F., Orville, H., Farley, R., Hirsh, J., 1983. Numerical simulation of dry ice cloud seeding experiment. J. Climate Appl. Meteor. 22, 1542–1556.

Lesins, G., List, R., 1986. Sponginess and drop shedding of gyrating hailstones in pressure-controlled icing wind tunnel. J. Atmos. Sci. 43, 2813–2825.

Lesins, G., List, R., Joe, P., 1980. Ice accretions. Part I: Testing of new atmospheric icing concepts. J. Rech. Atmos. 14, 347–356.

Lin, Y.-L., Farley, R.D., Orville, H.D., 1983. Bulk parameterization of the snow field in a cloud model. J. Atmos. Sci 22, 1065–1089.

Low, T., List, R., 1982. Collision, coalescence and breakup of raindrops. Part I: Experimentally established coalescence efficiencies and fragment size distributions in breakup. J. Atmos. Sci. 39, 1591–1606.

Meyers, M.P., DeMott, P.J., Cotton, W.R., 1992. New primary ice nucleation parameterizations in an explicit cloud model. J. Appl. Met. 31, 708–721.

Mossop, S.C., 1976. Production of secondary ice particles during the growth of graupel by riming. Quart. J. Roy. Meteorol. Soc. 102, 45–57.

Murakami, M., 1990. Numerical modeling of dynamical and microphysical evolution of an isolated convective cloud – The 19 July 1981 CCOPE cloud. J. Met. Soc. Jap. 68, 107–128.

Nickerson, E.C., Richard, E., Rosset, R., Smith, D.R., 1986. The numerical simulation of clouds, rain, and airflow over the Vosges and Black Forest Mountains: A meso-β model with parameterized microphysics. Mon. Wea. Rev. 114, 398–414.

Orville, H.D., Kopp, F.J., 1977. Numerical simulation of the life history of a hailstorm. J. Atmos. Sci. 34, 1596–1618.

Prodi, F., 1970. Measurements of local density in artificial and natural hailstones. J. Appl. Met. 9, 903–910.

Pruppacher, H.R. and Klett, J.D., 1978. Microphysics of clouds and precipitation. D. Reidel, 714 pp.

Rasmussen, R.M., Heymsfield, A.J., 1987a. Melting and shedding of graupel and hail. Part I: Model physics. J. Atmos. Sci. 44, 2754–2763.

Rasmussen, R.M., Heymsfield, A.J., 1987b. Melting and shedding of graupel and hail. Part II: Sensitivity study. J. Atmos. Sci. 44, 2764–2782.

Rasmussen, R.M., Heymsfield, A.J., 1987c. Melting and shedding of graupel and hail. Part III: Investigation of the role of shed drops as hail embryos in the 1 August CCOPE Severe Storm. J. Atmos. Sci. 44, 2783–2803.

Rasmussen, R.M., Levizzani, V., Pruppacher, H.R., 1984. A wind tunnel and theoretical study on the melting behavior of atmospheric ice particles III: Experiment and theory for spherical ice particles of radius > 500 μm. J. Atmos. Sci. 41, 381–388.

Rutledge, S.A., Hobbs, P.V., 1983. The mesoscale and microscale structure and organization of clouds and precipitation in midlatitude cyclones. VIII: A model for the 'seeder-feeder' process in warm-frontal rainbands. J. Atmos. Sci. 40, 1185–1206.

Rutledge, S.A., Hobbs, P.V., 1984. The mesoscale and microscale structure and organization of clouds and precipitation in midlatitude cyclones. XII: A diagnostic modeling study of precipitation development in narrow cold-frontal rainbands. J. Atmos. Sci. 41, 2949–2972.

Srivastava, R., 1978. Parameterization of raindrop size distributions. J. Atmos. Sci. 35, 108–117.

Stevens, B., Walko, R.L., Feingold, G. and Cotton, W.R., 1995. On the spurious production of cloud edge supersaturations by Eularian models. Mon. Wea. Rev., In press.

Verlinde, J., Flatau, P.J., Cotton, W.R., 1990. Analytical solutions to the collection growth equation: Comparison with approximate methods and application to cloud microphysical parameterization schemes. J. Atmos. Sci. 47, 2871–2880.

Verlinde, J., Cotton, W., 1993. Fitting microphysical observations of non-steady convective clouds to a numerical model: An application of the adjoint technique of data assimilation to a kinematic model. Mon. Wea. Rev. 121, 2776–2793.

Walko, R., Cotton, W.R., Meyers, M.P., Harrington, J.Y., 1995. New RAMS cloud microphysics parameterization. Part I: The single-moment scheme. Atmos. Res. 38, 29–62.

Wang, P.K., Chang, J.S., 1993. A three dimensional numerical model of cloud dynamics, microphysics, and chemistry 1. Concepts and formulations. J. Geophys. Res. 98, 14827–14844.

Young, K.C., 1974. A numerical simulation of wintertime, orographic precipitation. II: Comparison of natural and AgI-seeded conditions. J. Atmos. Sci. 31, 1749–1767.

Ziegler, C.L., 1985. Retrieval of thermal and microphysical variables in observed convective storms. Part I: Model development and preliminary testing. J. Atmos. Sci. 42, 1487–1509.